Seventh International Conference on Computational Fluid Dynamics (ICCFD7), Big Island, Hawaii, July 9-13, 2012

ICCFD7-4304

External Aerodynamics Simulations for the MIT D8 "Double-Bubble" Aircraft Design

Shishir A. Pandya
NASA Ames Research Center, Moffett Field, CA, USA

Abstract: The D8 "double-bubble" aircraft is a radical new design that may substantially reduce the fuel burn, noise, and emission of future commercial transportation aircraft. In order to independently verify some of the advantages proposed in this design, a study of the external aerodynamics of an unpowered version of the D8 aircraft is performed using Overflow, a viscous flow solver. Cart3D, an inviscid flow solver is used to conduct some preliminary analysis and to guide the viscous mesh generation. Various aspects of the modeling and simulation process, including geometry, mesh generation, solution procedure, and sensitivity to meshing parameters, are discussed. The computed lift and drag results are compared to a wind tunnel experiment. Some aspects of the design are also verified using the simulation results. The procedures established in this unpowered configuration study form the basis necessary to perform further detailed studies on this configuration, including the addition of nacelles and boundary layer ingesting engines.

Keywords: Cartesian, Overset, Aerodynamics, BLI, boundary-layer ingesting engine.

1 Introduction

The Subsonic Fixed Wing (SFW) project in NASA's Fundamental Aeronautics program is developing technologies and concepts to drastically improve the energy efficiency and environmental countability of the future commercial transport aircraft. The SFW project focuses on the 'N+3' timeframe (i.e. three generations beyond the current) with notional entry into service in approximately 2030-35. The project is leveraging both in-house and external expertise. The goal of the SFW 'N+3' solicitation was to stimulate thinking to address future issues, such as reducing energy consumption, environmental impact, and noise, and dealing with future operations challenges. To achieve this, the program is identifying advanced airframe, and propulsion systems concepts, and is working to bring enabling technologies to maturity.



Figure 1: The MIT D8 "double-bubble" concept aircraft.

This paper presents a study of the external aerodynamics characteristics of an aircraft design proposed by a team led by the Massachusetts Institute of Technology (MIT) that incorporates enabling technologies in response to the NASA 'N+3' solicitation. With potentially major performance benefits, the D8 (double-bubble) aircraft design [1, 2] is proposed as a Boeing 737 class aircraft that carries 180 passengers with a range of 3000 nmi (see Fig. 1). It is shorter than the 737-800 with a longer wingspan. The cruise speed of the D8 will be $M = 0.72$ which is lower than the 737's $M = 0.8$. The lower Mach number combined with a

fuselage design that acts as a diffuser for the engines results in the flow reaching the fan face at approximately $M = 0.6$. Since most engine fans are designed for this incoming flow speed, this minimizes the need for a large-inlet nacelle. The smaller nacelle means lower weight. However, one result of this engine placement is that a large part of the fan is in the boundary layer of the fuselage, requiring a distortion tolerant fan. Additionally, the fuselage can also be contoured to act as the lower part of the nacelle, further reducing weight. The empennage also contributes to weight reduction because the vertical pieces of the π-shaped tail can be used as the sides of the nacelle. This embedding of the engines into the rear of the fuselage and π-tail leads to a reduction in nacelle size and thus a reduction in nacelle drag as compared to a podded or under-wing nacelle.

Another advantageous design feature is the "double-bubble" fuselage itself. An increased amount of lift is generated by the fuselage along with a positive pitching moment at cruise conditions resulting in a smaller wing and horizontal tail. Once again, this results in a reduction in the weight of the aircraft. Additional reduction in weight comes from the wing of the aircraft due to a smaller sweep angle because of the lower cruise speed. These design features, combined with advanced materials, gains in efficiency due to the boundary layer ingesting engines [3], and the high bypass ratio small core engines, result in a highly efficient aircraft that meets the challenging performance metrics of NASA's SFW project.

The objective of this paper is to validate computational fluid dynamics (CFD) simulations of the unpowered configuration (without engines) against wind tunnel (WT) data obtained by MIT in order to establish a baseline prediction capability. Both inviscid and viscous computations are performed. Inviscid computations employed an adjoint-based mesh refinement procedure on an unstructured Cartesian mesh. The resulting inviscid mesh is used as a guide along with overset best practices to decide where to concentrate the mesh for the viscous computations. Viscous computations are performed using structured overset mesh technology. A study discussing geometry and the effects of various parts of the wind tunnel test model is presented after describing the methods employed. A baseline mesh is created and a mesh parameter sensitivity study is presented. An alpha-sweep at the wind tunnel Mach number is compared to experimental wind tunnel data obtained at MIT. A preliminary study of the effect of turbulence models on the forces and moments at high angles of attack is also presented. Finally, a few of the design assumptions behind the D8 aircraft and its preliminary performance estimates are assessed [1, 2].

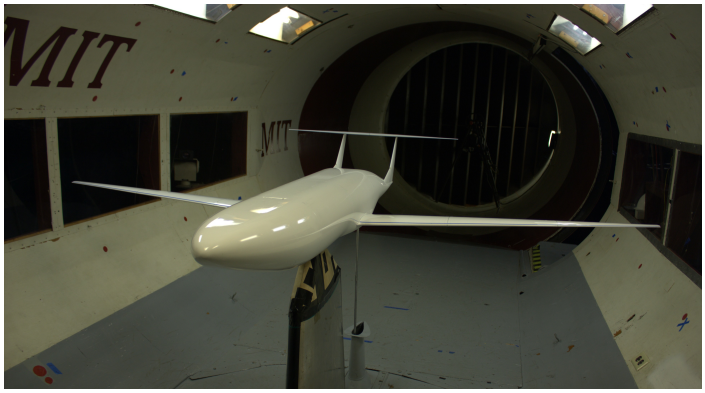


Figure 2: A photograph of the model in the MIT Wright brothers wind tunnel. (MIT)

2 Wind Tunnel Configuration

A 1:20 scale model of the D8 aircraft was slightly modified for low-speed conditions and tested in the Wright Brothers Wind Tunnel (WBWT) at MIT at 120 mph (see Fig. 2). The tests were performed at various angles of attack between 0 and 13 degrees. The wing of the test model has a mean chord of 6 inches. Based on this chord, the tests were performed at a Reynolds number of approximately $477,000$. Boundary layer trips were employed to assure turbulent flow on the wing, fuselage and tail surfaces.

To compare to this test, CFD simulations are performed at 120 mph (approximately $M = 0.16$) for angles of attack between -2 and 14 degrees in 2 degree increments. The solutions are non-dimensionalized by the mean chord (6 in.) and a reference area of 525 sq. in. for the full aircraft model. The geometry includes wind tunnel walls and the mounting hardware in the wind tunnel (see Fig. 3). However, simulations without the mounting strut and in free air are also performed to assess the need for including these for comparison with wind tunnel data. Due to symmetry considerations, only the right half of the airplane is modeled in

the CFD simulations, thus lowering the number of grid points required and halving the computational cost. Care is taken to represent the geometry as closely as possible with two exceptions. First, the wind tunnel walls are modeled as an extension of the test section walls. Thus, the CFD meshes cover the test section accurately, but extend it up- and down-stream in order to model the flow inside the wind tunnel. Second, no attempt is made to model small pieces of hardware such as the load balance rod between the mounting strut and the trunnion that supports the D8 model.

3 The D8 Geometry

3.1 Sources of Geometry

The D8 reference geometry was obtained from MIT and resulted in four reference surface representations. First, a CAD model of the geometry was provided from the EGADS CAD system [4]. Along with the CAD, a coarse triangulation was also provided. This coarse triangulation became the reference geometry for the first set of meshes. The solutions from this first reference geometry are reasonable, but resulted in pressure coefficient (C_p) plots in a span-wise cut plane ($y = 20$ in.) that are oscillatory in the vicinity of the leading edge, where x is the stream-wise coordinate, y is the span-wise coordinate along the right wing and z is pointed upwards.

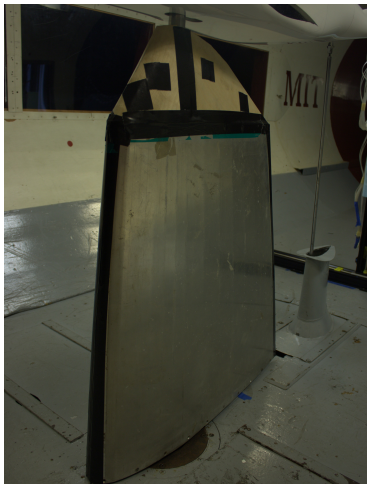


Figure 3: A photograph of the mounting hardware in the MIT Wright Brothers wind tunnel. (MIT)

To obtain a less oscillatory solution, a second geometry reference was created by obtaining a finer triangulation from the CAD model. The resulting solutions are smoother, but contain minor oscillations on the lower surface near the leading edge, and the upper surface near the trailing edge. The oscillations are a result of the fact that smoothness across triangles could not be guaranteed. Thus, a decision was made to bypass the CAD model and to create meshes from the panel network used to create the CAD model.

This original panel network was coarse and so a reference geometry is obtained from it by splining through its points along the surface. The resulting reference surface is smooth, but lacks geometric fidelity in the portions that are very coarse. As a result, the solutions obtained with this geometry are smoother near the leading and trailing edges. However, they are not as smooth on top and bottom surfaces of the wing due to splining errors.

For this reason, a finer set of panel networks was obtained from MIT, which resulted in the final reference surface used for this study. This final reference geometry is smooth and provides a set of smooth C_p cuts along a section of the wing as shown in Fig. 4.

While the C_p values are substantially effected by the variations in the airfoil representations from the four sources of geometry, the effect of the oscillations in the solution on integrated forces also needs to be investigated. A general similarity in the resulting viscous overset mesh is enforced resulting in a mesh with between 80 and 85 million grid points regardless of the fact that the fidelity of the reference surface geometry varies greatly. The original mesh has a reference surface with approximately 1.2 million triangles, while the finer triangulation from CAD has approximately 4.9 million triangles. The coarse panel network has approximately 2700 faces as compared to the fine panel network, which has approximately $280,000$ faces.

Table 1 shows the C_L and C_D values for the D8 aircraft obtained from the four sources of geometry. It can be seen that the integrated forces are minimally effected by the geometric variations.

3.2 Wind Tunnel Walls and Mounting Hardware

To assess the importance of modeling the wind tunnel walls and mounting hardware in the wind tunnel, an inviscid study is carried out. The highly dissipative Minmod limiter is used to keep the solutions from

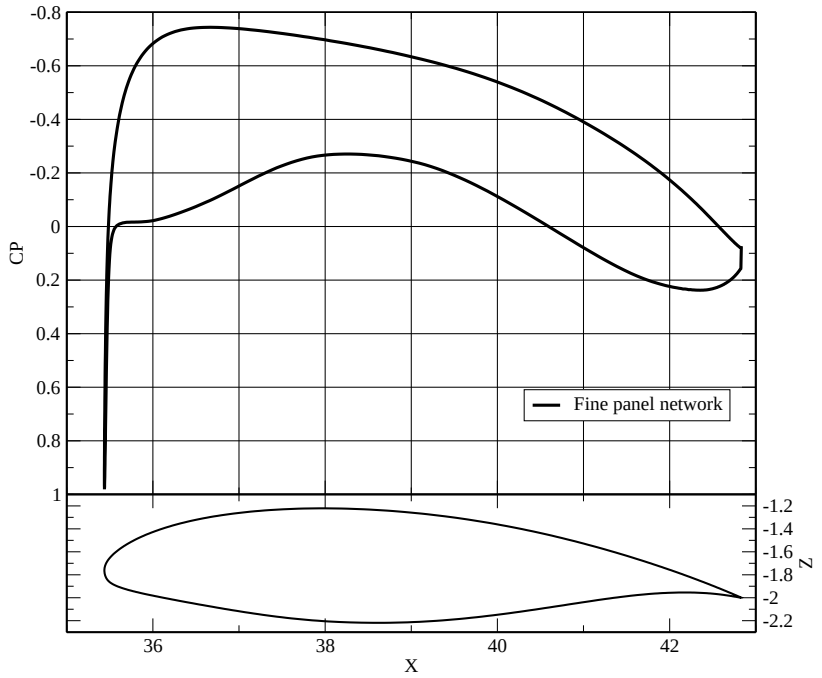


Figure 4: Surface pressure coefficient along the $Y = 20$ inches (44%) span-wise cut.

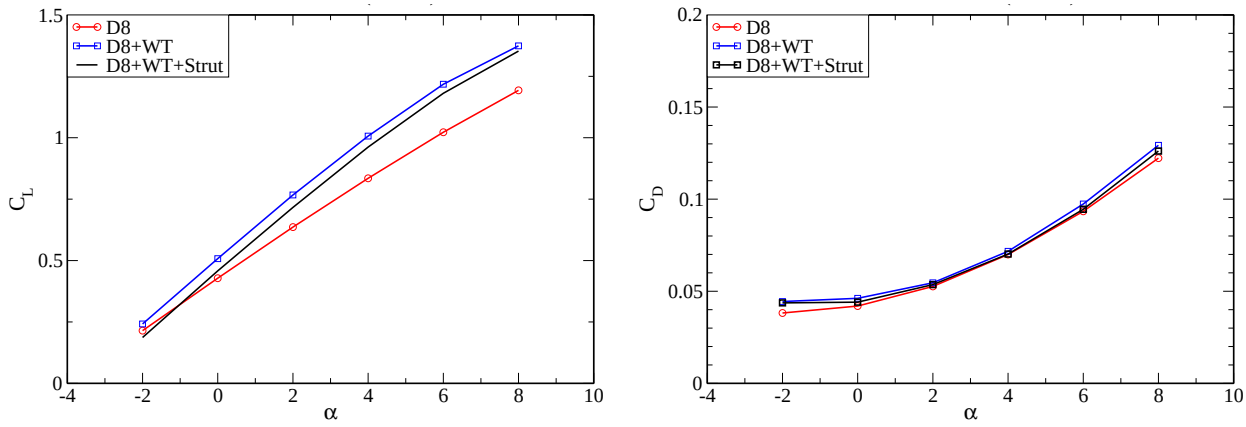
Table 1: Comparison of lift and drag coefficients for various geometry representations.

	Triangulation		Panel network	
	Coarse	Fine	Coarse	Fine
C_L	0.4393	0.4507	0.4560	0.4553
C_D	0.0348	0.0358	0.0358	0.0358

oscillating at high angles of attack. While this method provides a good understanding of the importance of the wind tunnel walls and mounting hardware, the solutions are too dissipative and cannot be used for code-to-code comparison of lift and drag coefficients. Figure 5(b) shows that the drag does not vary substantially with the presence or absence of the wind tunnel walls or the mounting hardware. This is expected since the wind tunnel wall and hardware blockage is not expected to change the pressure on the leading and trailing edges of the wing and other surfaces. However, such blockage can have a substantial effect on the lift due to change in pressure above and below the wing from the additional blockage. Figure 5(a) shows the variation of the lift coefficient as a function of the angle of attack for the three cases: free air, with WT walls, and with WT walls and mounting strut. The figure shows that the lift is substantially higher with the wind tunnel wall than without. Thus, for proper quantitative and trend comparison of the WT and CFD data, the WT walls cannot be neglected. Furthermore, Fig. 5(a) also illustrates the effect of the mounting hardware. It can be seen that the mounting hardware reduces lift for most of the lower angles of attack making it necessary to include the strut under the aircraft model in the computations.

4 CFD Methodology

The Cart3D code is used with its adjoint-based mesh refinement Aero module [5] to obtain inviscid solutions for the D8. The resulting solutions are used for preliminary analysis and to assess the need for wind tunnel walls and mounting hardware. Solutions for low angles of attack are used for code-to-code comparisons and the resulting solution adapted grids are used to obtain some preliminary guidance for the viscous grid generation process. Structured overset mesh technology [6] is used to perform viscous simulations for the D8 configuration. The Chimera Grid Tools' (CGT) package is used to generate surface and volume meshes and



(a) C_L (b) C_D

Figure 5: Comparison of lift and drag force coefficients as a function of the angle of attack with and without wind tunnel walls and mounting hardware from Cart3D inviscid simulations.

the Overflow code [7] is used to obtain viscous solutions on the resulting meshes. The resulting solutions are compared to the MIT wind tunnel experiment for validation.

4.1 Inviscid Simulations

The Cart3D process begins with a triangulation obtained from the CAD definition of the D8 using the CAPRI tool [8, 9]. The fuselage, wing, and the vertical and horizontal pieces of the π-tail are triangulated separately. The components are placed at the correct location with respect to each other and a slight overlap between the components is assured. The components are intersected to obtain the triangulation for the full aircraft configuration. The wind tunnel walls and mounting hardware are created from an engineering drawing as panel networks which are then triangulated for Cart3D. These surface triangulations are then provided as input to the Cartesian mesh generation system, which generates a preliminary coarse Cartesian embedded mesh through subdivision of an initial uniform hexahedral cell grid. It adapts to the contours of the geometry so that the mesh remains coarse away from the geometry, but cells close to the geometry are refined. Intersections of the hexahedra that cut the geometry are computed to obtain polyhedral cut-cells.

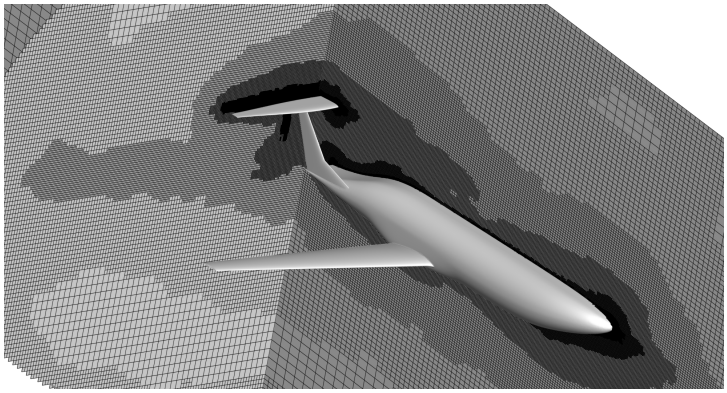
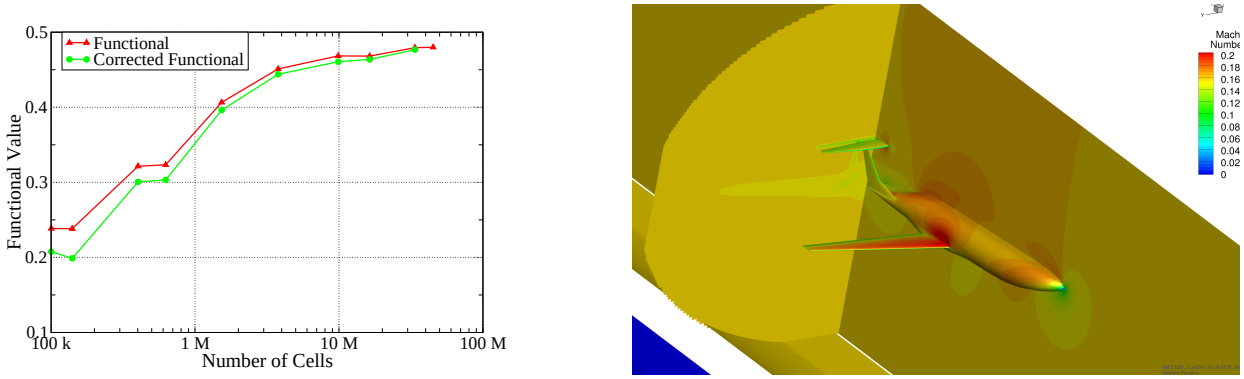


Figure 6: An automatically refined Cartesian embedded mesh for the D8 inviscid runs.

A solution is now obtained on this initial coarse mesh using an efficient upwind, multi-grid procedure with Runge-Kutta time marching and the van Leer limiter. The solution on the initial mesh is automatically refined using an adjoint solution to predict regions that are sources of error for a given functional (a combination of C_L and C_D). The process is repeated a desired number of times to obtain a final solution-adapted mesh. An example of a refined mesh around the D8 with WT walls can be seen in Fig. 6 and shows clustering of the mesh near the body, in the wing wake, and in the vicinity of the empennage where aerodynamic interference is expected. For most inviscid simulations, 9 adapt cycles were employed. A typical convergence of the functional is shown in Fig. 7(a) where the red curve shows the actual converged value of the functional at each cycle and the green curve shows the future predicted value based on an estimate of the error. A typical solution resulting from this process is also shown in Fig. 7(b).



(a) Convergence of the adjoint functional.

(b) Typical solution (Mach number contours).

Figure 7: Adjoint convergence and a typical solution.

4.2 Viscous Simulations

The viscous simulation process begins with either a reference surface triangulation or a reference panel network that defines the surface of the body. Various CGT tools are accessed through the scripting library [10] to generate an overset structured surface mesh on each component of the aircraft. A collar grid is generated to discretize the volume around intersections between components (e.g. wing-fuselage junction). These overset surface meshes constitute the inputs to the volume mesh generation process. A hyperbolic mesh generation code in CGT [11] is used to generate the near-body volume meshes for the components of the D8 as well as for the WT walls and the mounting strut. To cover the space between the near-body grids and the WT wall grid, a set of Cartesian box grids is generated. Finally, the volumes up- and down-stream of the test section are covered with a core grid that follows the shape of the outer shell of the WT grid. Each step of the mesh generation process follows the overset mesh generation best practices [12] to decide the size of the grid cells and the amount of overlap between two overlapping grids.

The solution-adapted Cart3D mesh is also used to guide the mesh density in some of the off-body grids. The fact that the inviscid adjoint process indicates a substantial amount of refinement in the fuselage/empennage interaction region means that a finer box grid is needed to cover that part of the volume. Furthermore, the additional refinement in the wing wake prompted the use of a specialized wake grid to capture the flow (shown in Fig. 9(a)). The wake grid overlaps the wing grid up to the trailing edge. It extends from the trailing edge to several chord lengths behind the wing. The wake grid has fine spacing at the trailing edge in all directions, but follows the same spacing as the wing mesh in the span-wise direction. In the normal direction, the spacing is determined based on the viscous spacing needed to capture the wake. The spacing remains at that value for some distance above and below the trailing edge, and stretches after that. The mesh also stretches in the downstream direction. This type of mesh is able to properly cluster points in the wake region, which is an advantage over the standard o-mesh topology. An additional benefit of this specialized mesh is that one can cluster the mesh near the wing tip to capture the tip vortex in more detail. The resulting wake and tip vortex are shown in Figs. 9(b) and (c).

The resulting mesh is input into the Overflow code, along with initial and boundary conditions to obtain viscous solutions for the D8 external aerodynamics. The internal X-rays module [13] of the Overflow code is used to obtain mesh connectivity and interpolation coefficients to facilitate communication between two overlapping grids.

Using the overset best practices and the preliminary guidance from the Cart3D adapted mesh, a baseline mesh is developed with a target y^+ of 1 with a uniform layer of cells next to the body. A near-wall stretching ratio of 1.15, off-body spacing of 0.3 inches, and surface spacing parameter that corresponds to a leading edge spacing of 0.1% of the mean chord are used. The trailing edge spacing is generally set to half the leading edge spacing which corresponds to a surface mesh which had approximately 550 points defining the root airfoil and 300 points defining the tip airfoil with the mesh stretching to coarser spacing in flatter regions compared to the leading and trailing edges. The resulting baseline mesh, shown in Fig. 8, is 35 overset volume meshes containing approximately 80 million points for the D8, WT walls, and mounting strut.

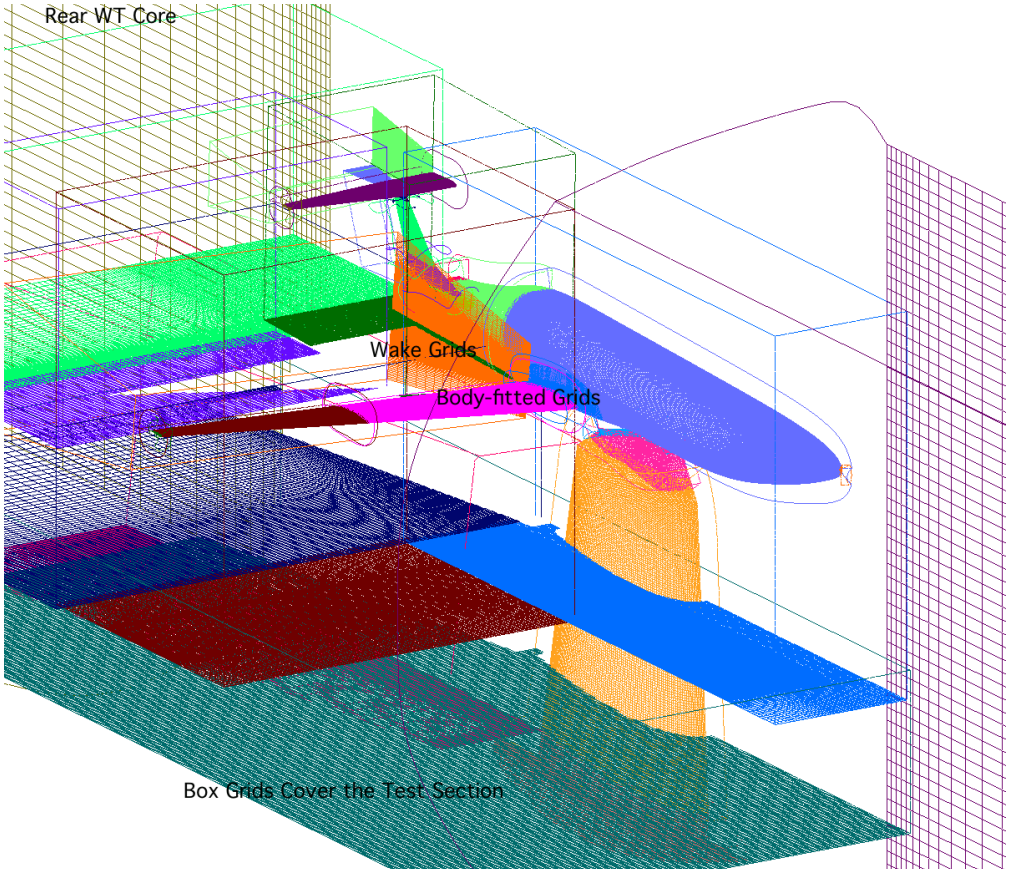
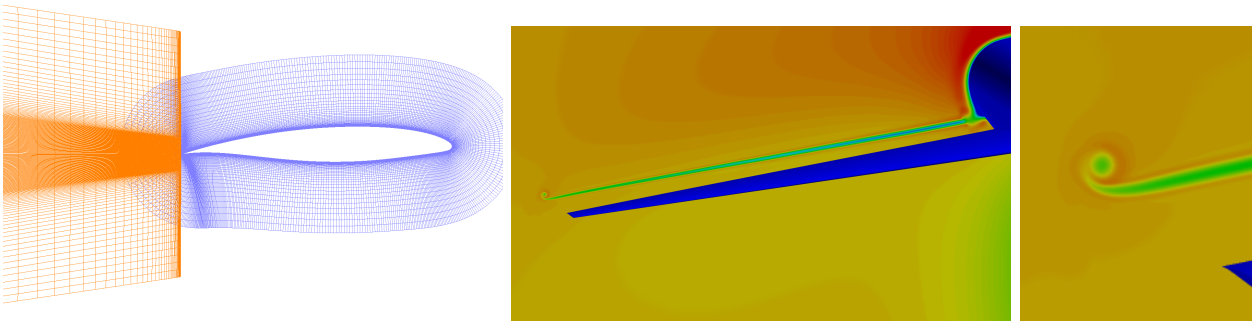


Figure 8: The anatomy of the overset mesh used for the Overflow viscous simulations.

Several consistency checks are performed to assure that the solution methodology is accurate. A comparison of various methods of solving the left hand side reveals that the Beam-Warming approximate factorization scheme [14] is the most robust. The integrated forces using three other schemes (the Pulliam-Chausee diagonalized scheme [15], Roe [16], and HLLC [17, 18]) are computed. The results show a maximum variation of 3% in the lift coefficient and 1.4% in the drag coefficient when converged to approximately 5 orders of magnitude. This level of variation due to changes in scheme is expected because of the varying amount of dissipation in each scheme. The flow behavior is further investigated by running the code in unsteady



(a) 2D slice of a wing and wake grid.

(b) Planar cut behind the wing showing the wake and tip vortex.

(c) Zoom-in view of the tip vortex.

Figure 9: A specialized mesh for capturing the wake and tip vortex.

mode to determine if there is any unsteadiness present in the flow field that is not captured by the steady algorithm. No unsteadiness is found. Inquiry into the use of various boundary conditions to model the wind tunnel inlet and exit faces resulted in minimal changes to the solutions with lift varying less than 1.5% and drag variations below 1%. Finally, the low Mach number pre-conditioner is turned on to assure that no low-Mach effects are contaminating the solution given the low free-stream Mach number. No changes are found in the integrated force coefficients due to the low-Mach number pre-conditioner.

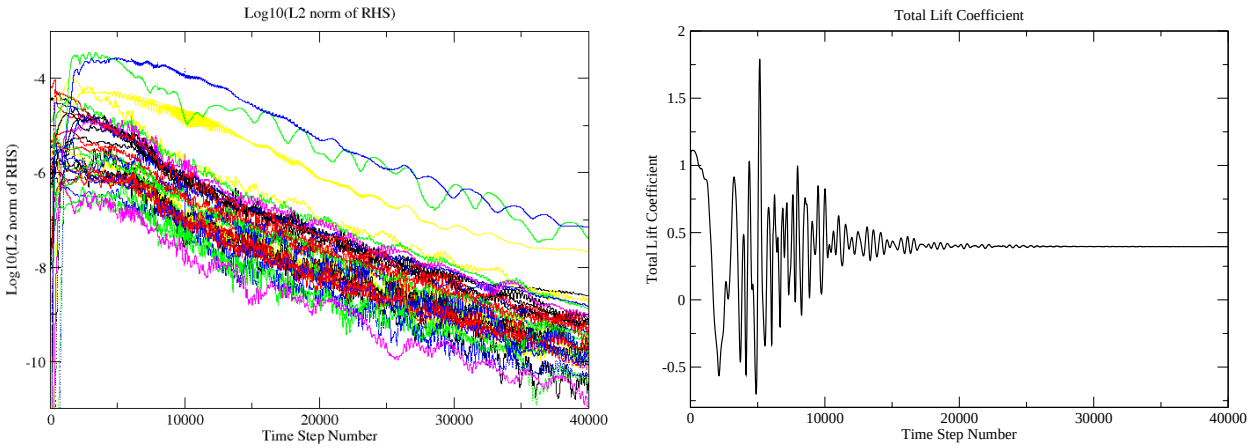
As a result of these consistency comparisons, all computations performed with the Overflow code in this study use the Beam-Warming approximate factorization scheme in steady mode without a low-Mach number pre-conditioner. The wind-tunnel walls are modeled as inviscid wall boundaries since the WBWT walls are tapered to compensate for boundary layer growth. The spatial accuracy of the central-difference right-hand side is formally second order. The Spalart-Allmaras turbulence model [19] is chosen as it is considered appropriate for attached flow over wings. A typical solution convergence of the resulting solution process is shown in Fig. 10. The L2-norm of the right-hand-side residual is plotted for all grids and it can be seen that all grids converge approximately 4 to 5 orders of magnitude. Typical solutions on the top and bottom of the aircraft are shown in Figs. 11(a) and (b) respectively.

5 Solution Sensitivity to Mesh Parameters

A solution sensitivity study is carried out at an angle of attack of zero degrees to see if the integrated forces are independent of meshing parameters. Four major parameters are tested independently, namely the wall spacing (target y^+), surface spacing (wing leading edge spacing, trailing edge spacing, and global spacing parameters on the surface), near-wall stretching ratio, and off-body spacing. The meshes for this study are generated using mesh parameters close to the baseline mesh.

5.1 Sensitivity to y^+

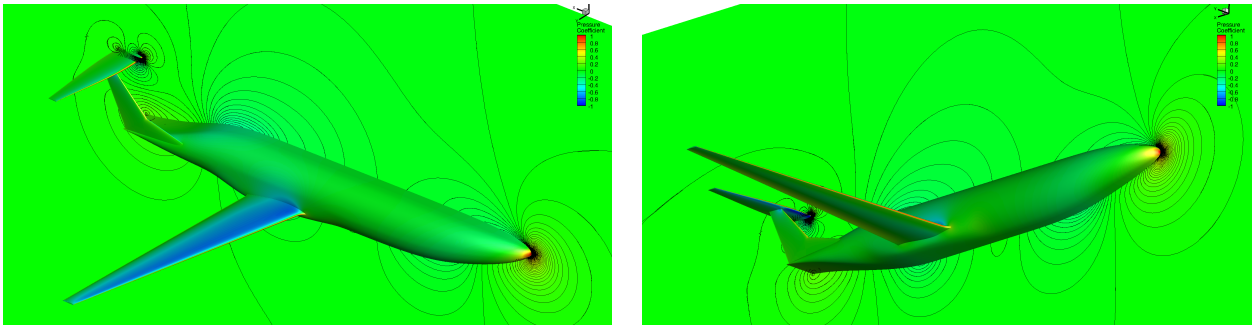
Figures 12(a) and (b) show the lift and drag coefficients respectively to illustrate the dependence of the integrated forces on y^+. Turbulence model developers generally recommend that while a y^+ of below 5 is adequate in most cases, a safe value of $y^+ = 1$ should be regarded as an appropriate wall spacing for most turbulence models [20]. To verify this assertion, all other meshing parameters are held constant at a stretching ratio of 1.15, surface spacing reference of 1, and off-body spacing of 0.15 inches. The y^+ value is varied from 5 at the high end to 0.5 at the low end. It can be gleaned that above a value of $y^+ = 1$, the integrated forces change substantially; while below $y^+ = 1$, the integrated forces are minimally sensitive. This is verified by plotting the percentage change in the solution with respect to the number of grid points



(a) Residual.

(b) Lift.

Figure 10: A typical convergence in Overflow.



(a) View of top.

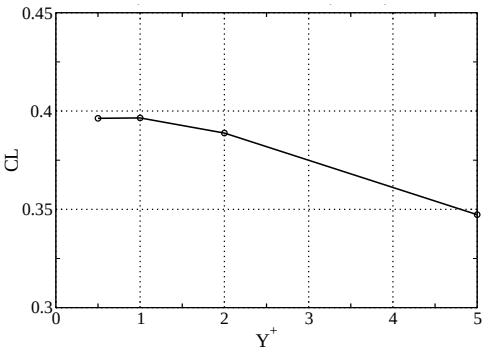
(b) View of bottom.

Figure 11: A typical Overflow solution on the D8 aircraft (pressure contours).

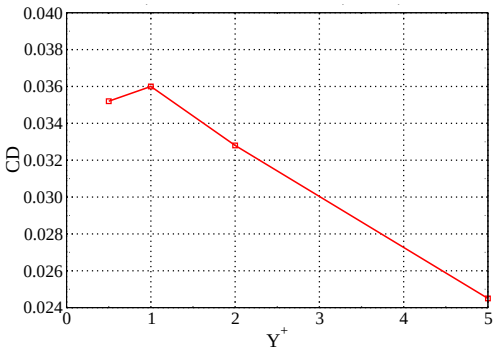
as shown in Fig. 12(c) and (d). These plots show that the variation in the solution below a y^+ of 1, which corresponds to approximately 80 million grid points, is close to 0% for C_L and approximately 2% for C_D. A y^+ of 1 is thus seen as adequate for obtaining a trustworthy solution.

5.2 Sensitivity to Surface Spacing

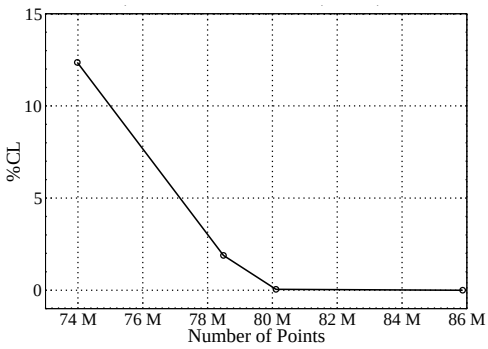
The spacing at the leading and trailing edges is very important in capturing the flow field changes in the vicinity of these geometric features [12]. The spacing on the flatter parts of the geometry can be important, for instance for flows with shocks, but at the low Mach number of 0.16 much larger spacings can be used. Thus, a reference value for the surface spacing is used since many surface meshing parameters are changed



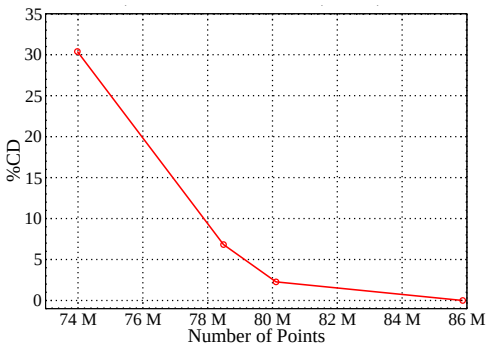
(a) C_L



(b) C_D



(c) $\%C_L$



(d) $\%C_D$

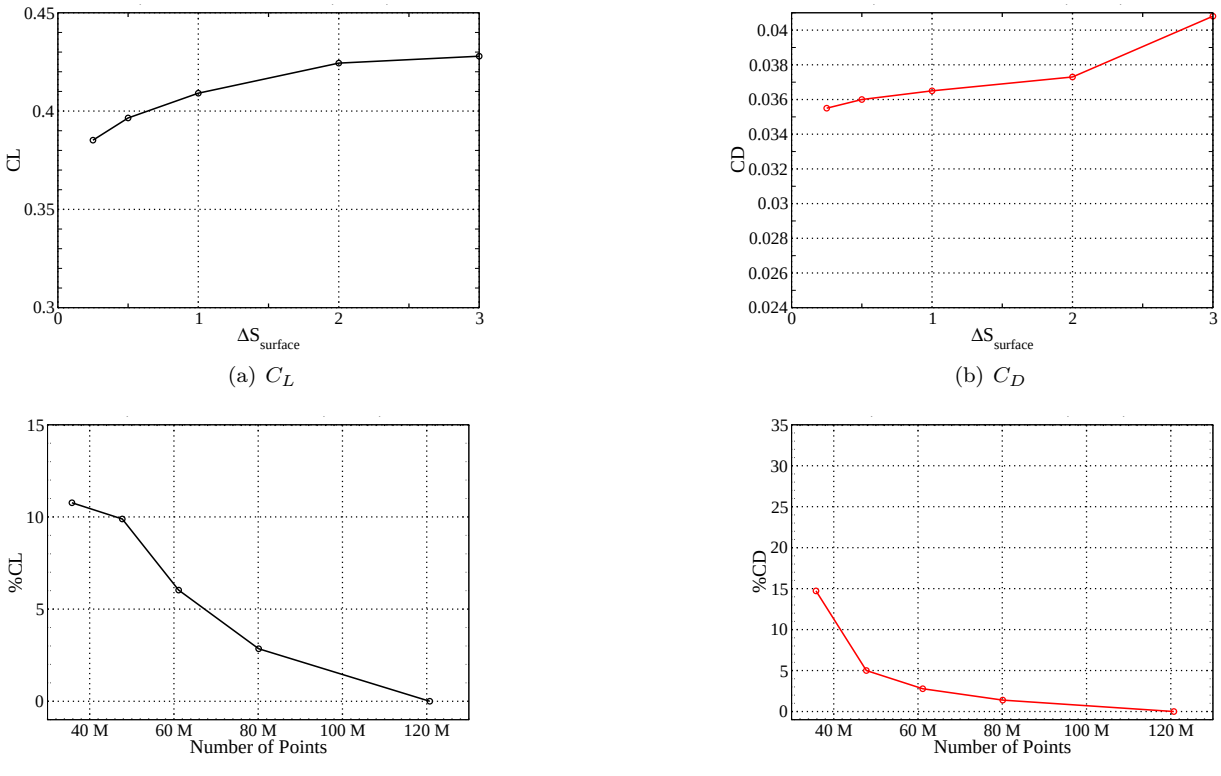
Figure 12: Sensitivity of the lift and drag coefficients to wall spacing (y^+) in Overflow viscous simulations.

as a function of this reference value to refine or coarsen the mesh. A reference value of 1, for example, means that the wing has a spacing of 0.1 inches (1.6% of chord) in the middle of the top and bottom surfaces and the leading edge is 0.006 inches (0.1% of chord). Because the ratio of the wing root chord to tip chord is on the order of 5, it is not reasonable to use the same spacing at the root and tip as the mean chord location. Thus, the root parameters are coarser and the tip mesh is created with finer spacings. All other surfaces (e.g. fuselage, π-tail) follow similar surface mesh spacing rules and are a function of the same reference value.

Figures 13(a) and (b) show the lift and drag coefficients respectively as a function of the surface spacing to illustrate the dependence of the integrated forces on the density of the surface mesh. The value of the reference surface spacing parameter is varied between 0.5 and 3. All other meshing parameters are held constant at y^+ of 1, a stretching ratio of 1.15, and off-body spacing of 0.15 inches. It can be seen from Fig. 13 that while the drag coefficient settles to a value below a surface reference spacing of 2, lift coefficient is changing substantially. Figures 13(c) and (d) show that while the drag converges to below 2% for the second finest mesh, the lift has an error as high as 3.5%. Thus it is concluded that the fine mesh reference value of 0.5 is necessary to obtain dependable results and further refinement may be necessary for future computations.

5.3 Sensitivity to Near-wall Stretching Ratio

The near-wall stretching ratio is important for providing proper resolution to capture the boundary layer. A high stretching may not provide enough resolution. However, too large a number of points may unnecessarily increase the cost of computing a solution. Thus, properly stretching the mesh away with increasing distance from the wall is necessary. The overset best practices suggest an appropriate amount of stretching at a ratio of 1.2 between two successive cells along an edge going away from the body [12]. Thus, we test stretching ratios between 1.1 and 1.25 while holding the y^+ at 1, the surface spacing reference value at 0.5 and the off-body spacing at 0.15. Figure 14 shows the results from this sensitivity study plotted on the same scale as

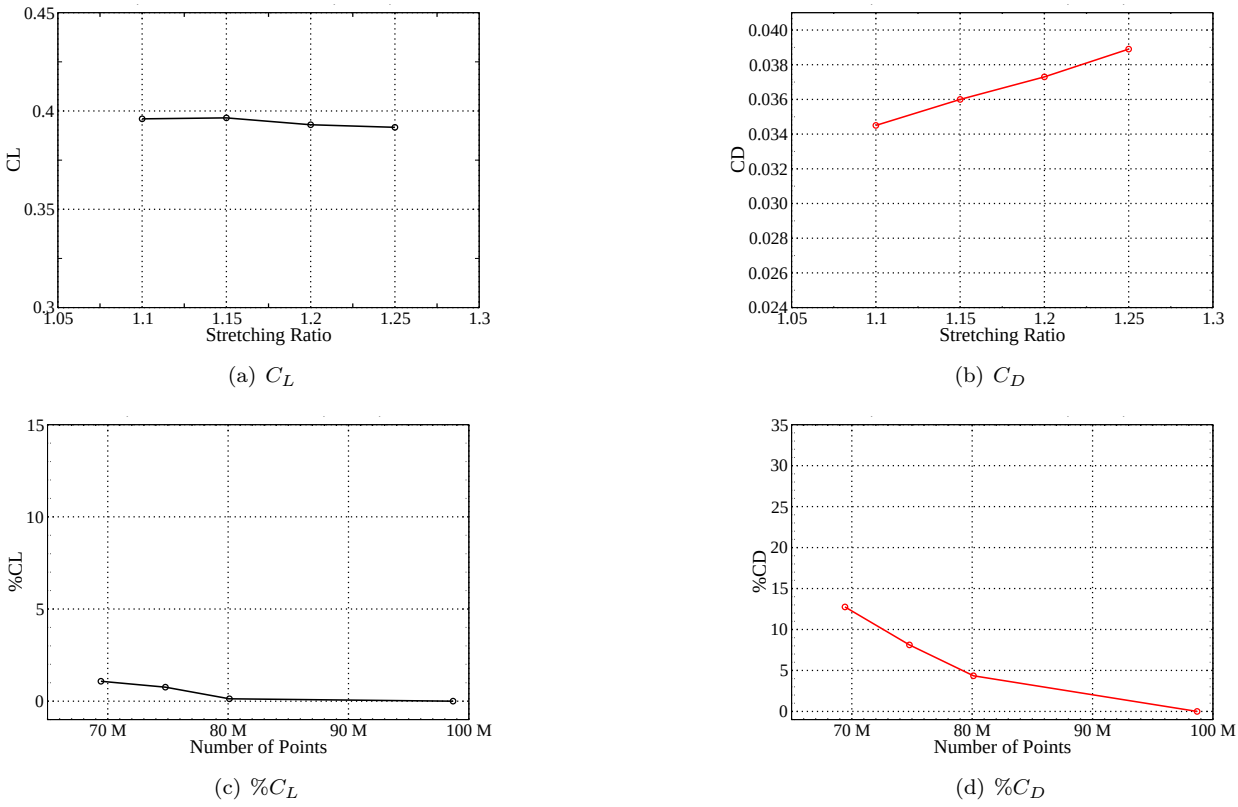


(a) C_L (b) C_D

(c) $\%C_L$ (d) $\%C_D$

Figure 13: Sensitivity of the lift and drag coefficients to surface mesh spacing in Overflow viscous simulations.

the previous two sensitivity studies (y^+ and surface refinement). It can be seen from Figs. 14(a) and (b) that the integrated forces do not change very much compared to previous parameters. Thus, we conclude that the effect of the stretching ratio on the solution is secondary compared to y^+ and surface spacing. It should also be noted that while the lift coefficient converges at a stretching ratio of 1.15, the drag coefficient is reduced almost linearly with respect to a reduction in stretching ratio. Figure 14(c) shows that the solution does not change between the two finest grids at stretching ratios of 1.1 and 1.15. The change in drag coefficient, however, is also observed to be of the order of 5%. While our baseline mesh uses a value of 1.15 for the stretching ratio, this may need to be revised for further confidence in drag.



(a) C_L (b) C_D

(c) $\%C_L$ (d) $\%C_D$

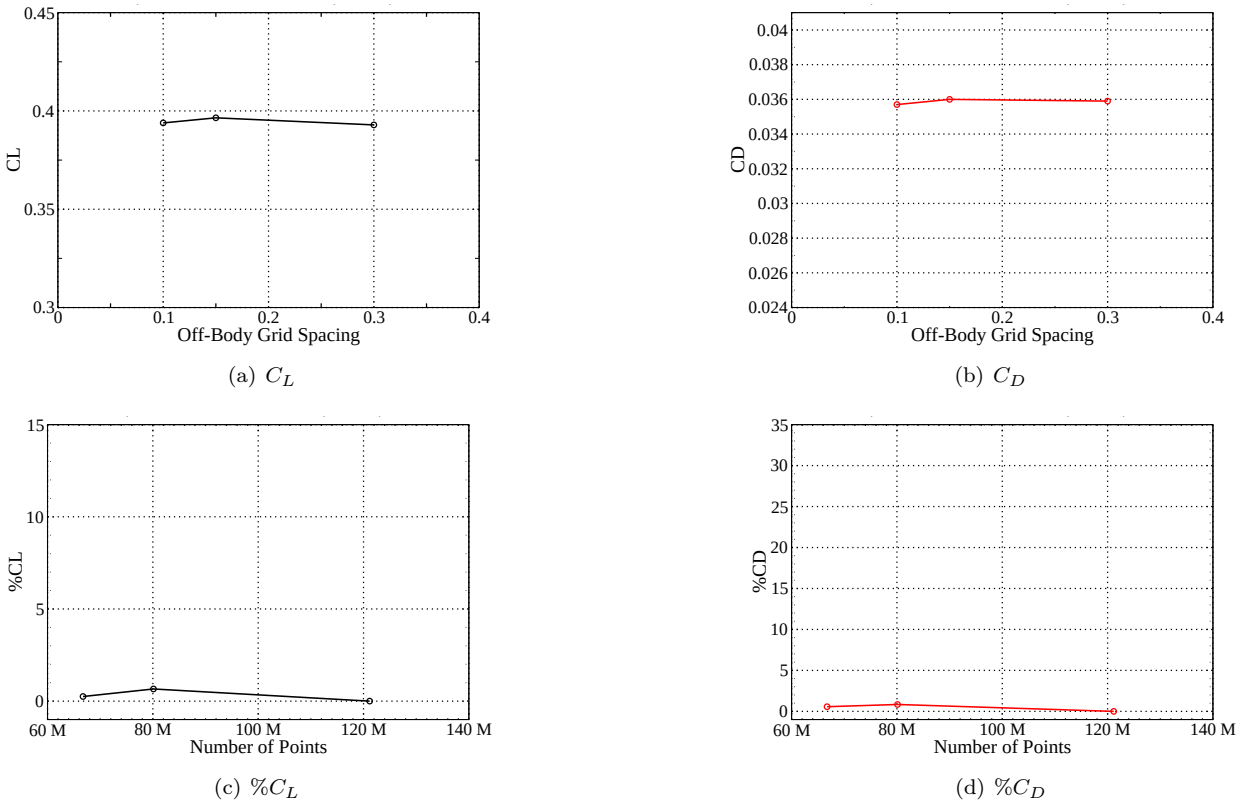
Figure 14: Sensitivity of the lift and drag coefficients to stretching ratio in Overflow viscous simulations.

5.4 Sensitivity to Off-Body Spacing

There are several types of off-body meshes in the computations. The open space in the test section region that is not covered by the near-body or wind tunnel meshes is where most of the off-body box grids reside. The spacing in these grids is specified by an off-body spacing parameter. The core meshes upstream and downstream of the test section also derive their grid spacing guidance from the off-body spacing. Other off-body meshes such as the wake meshes determine their grid spacings based on the near-body grid spacings of the component whose wake they are capturing (e.g. wing, horizontal tail, vertical tail). However, all near-body meshes get their far-field spacing (the spacing farthest from the body) from the off-body spacing parameter to assure commensurate spacing in the overlapping mesh region [12].

To assess the effect of this off-body spacing parameter on the integrated forces, values of 0.1, 0.15, and 0.3 are tested. The results are shown in Figs. 15(a) and (b). The variation due to the off-body spacing is minimal compared to the changes in y^+ or the surface spacing. Thus, changes in off-body spacing have a secondary effect on the integrated forces. Furthermore, Figs. 15(c) and (d) show that the percent variation of the integrated forces with respect to the finest mesh is less than 1% in all cases. Thus, the coarsest mesh, which corresponds to a value of 0.3 and approximately 65 million points, seems adequate. However, in the

absence of more rigorous testing at various angles of attack, the baseline mesh value of 0.15 is used for running the alpha sweep cases.



(a) C_L (b) C_D

(c) $\%C_L$ (d) $\%C_D$

Figure 15: Sensitivity of the lift and drag coefficients to off-body spacing in Overflow viscous simulations.

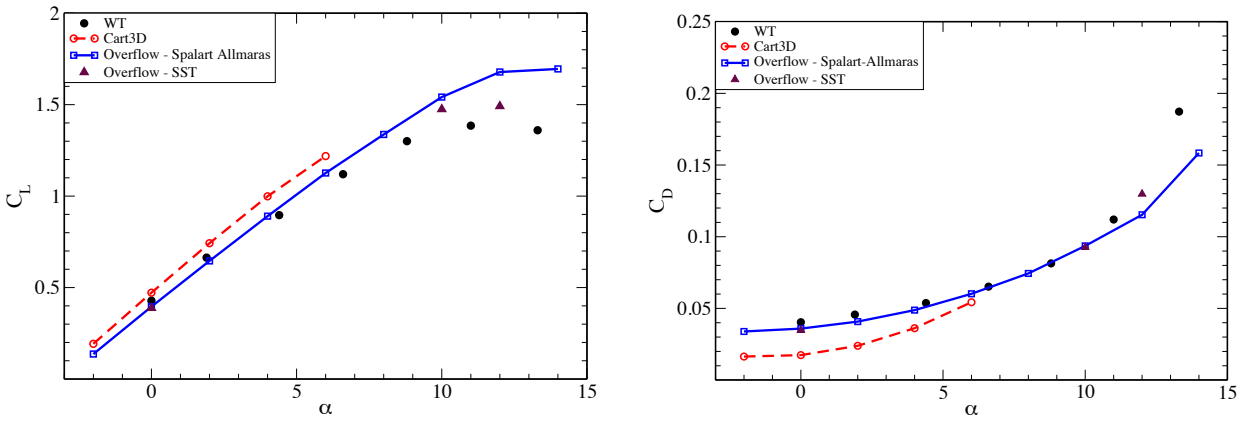
6 Results

The computational results from both inviscid and viscous simulations are presented and compared to the MIT wind tunnel experiment at $M = 0.16$ for angles of attack between -2 and 14 degrees. The integrated lift and drag coefficients are compared to the wind tunnel results and the trends are discussed. Furthermore, an independent assessment of the assertions claimed for the D8 design [1, 2] are briefly examined.

Figure 16(a) shows the lift coefficient as a function of angle of attack. Cart3D and Overflow solutions are compared to the wind tunnel results. The lift coefficients from the Cart3D and Overflow results compare well to the experimental results with Cart3D predicting slightly higher lift than the wind tunnel values at low angles of attack and Overflow resulting in a higher lift at high angles of attack. The steady Cart3D simulations become oscillatory above an angle of attack of 6°. This makes it difficult to converge to a value, thus the lift coefficient values from Cart3D are not reported above this α.

The drag comparison for the same α sweep is shown in Fig. 16(b). The drag prediction from Cart3D is lower than the WT data and the Overflow results owing to the fact that it does not include the viscous drag. Once again, the Cart3D solutions at higher angles of attack are not reported. The Overflow results are very close to the WT data with the SST turbulence model matching the experiment better at $\alpha = 12°$.

At higher angles of attack, the stall exhibited by the wind tunnel experiments is seen to occur at a higher angle of attack in the Overflow results with Spalart-Allmaras turbulence model. This results from delayed separation on the top of the wing and suggests that there may be turbulence modeling issues. To attempt to address these issues, simulations at 0°, 10°, and 12° are conducted with the Menter-SST turbulence model [21]. Figure 17 shows the stream-wise velocity contours in the $y = 20$ inches (44% of half-span) planar cut across the wing for the $\alpha = 12°$ case. The separated flow region, shaded blue, contains the negative



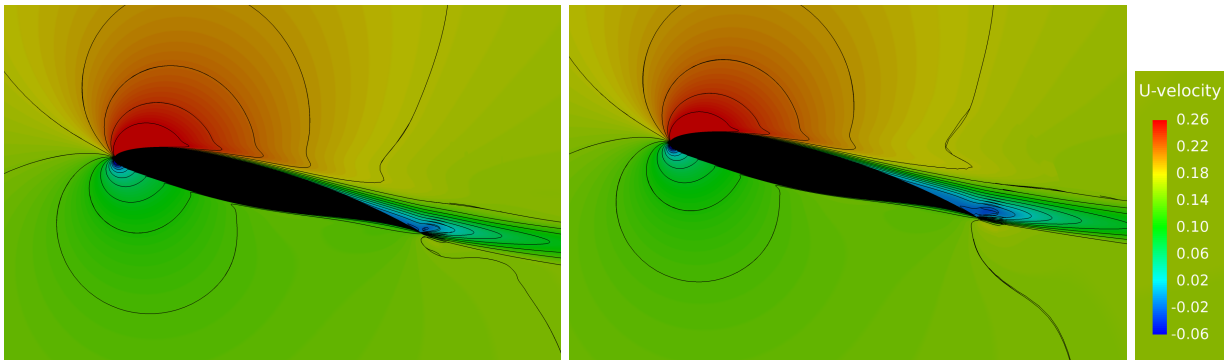
(a) C_L (b) C_D

Figure 16: Comparison of lift and drag coefficients (Cart3D inviscid CFD, Overflow viscous CFD and MIT wind tunnel experiment). The vehicle is modeled with wind tunnel walls and mounting hardware.

velocity contours. Fig. 17(a) shows the contours for the Spalart-Allmaras turbulence model. In this figure, the separation region is confined to a very small area on the rear, top part of the airfoil. This indicates that while stall is imminent, the flow has not separated significantly at this condition. Figure 17(b) shows the same cut for the SST turbulence model. The separated flow region predicted by the SST model is much larger. This larger separation should correspond to a stall. Figure 16(a) shows the lift coefficient from the SST computations with triangular symbols. It can be seen that the lift is indeed lower and closer to the WT values, indicating that the SST turbulence model is a better method for predicting the forces observed in the wind tunnel.

Next, we examine several assertions made in the design of the D8. The first assertion investigated is that the fuselage carries a substantial load [1, 2]. This can be verified by plotting the span-wise loading on the fuselage and comparing it to the wing. Figure 18 shows that the fuselage indeed carries a load similar to the wing. However, the load drops off at the fuselage/wing junction. The assertion is quantified by computing the lift generated by the fuselage and comparing it to the lift generated by the wing. Fig. 19 shows that the fuselage carries approximately 14% of the lift at 4 degrees angle of attack.

In reference [1], Drela predicts the loading on the π-tail to be slightly negative. This prediction is verified by the results obtained in our analysis, as shown in Fig. 18. One further detail is observed in the CFD calculations, which show a break in loading at the vertical portions of the π-tail indicating a higher negative load on the inboard part of the π-tail.



(a) Spalart-Allmaras (b) Menter-SST

Figure 17: Comparison of flow separation with turbulence models. Contours of stream-wise velocity are shown on the $Y = 20$ inches (44% half-span) airfoil cut for the $\alpha = 12°$ case.

Reference [1] also reports a positive (nose-up) pitching moment produced by the fuselage. It can be seen in Fig. 19 that the C_m from the fuselage is indeed positive and it is more positive for $\alpha = 4°$ than the $\alpha = 0°$ case.

Finally, the assertion that the rear part of the fuselage acts as a diffuser, thus lowering the inlet Mach number is examined. Figure 20 shows Mach number contours on a cutting plane and velocity profiles at three locations along the fuselage on the rear of the D8 aircraft in free-air at $M = 0.72$ and $\alpha = 4°$. A part of the π-tail is removed so that the flow in the rear is visible. A cartoon of the engine is also added to illustrate the approximate location of the fan face. The velocity profiles in Fig. 20 show that the boundary layer indeed thickens in the rear of the fuselage. The contours of the Mach number show that the speed of the flow is also reduced near the fan face with approximately half of the fan in the boundary layer. This shows that the fuselage is indeed acting as a diffuser and that the assertion that the flow speed will reduce

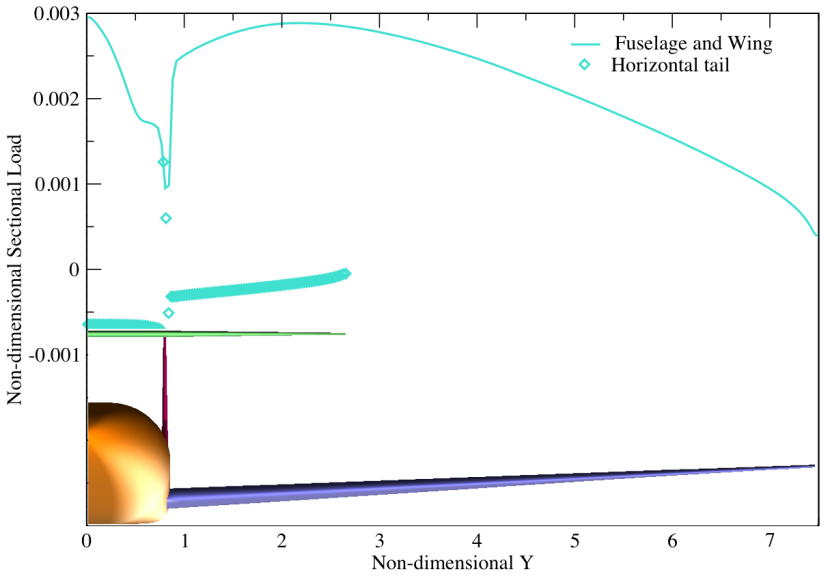


Figure 18: The computed span-wise loading on the D8 aircraft.

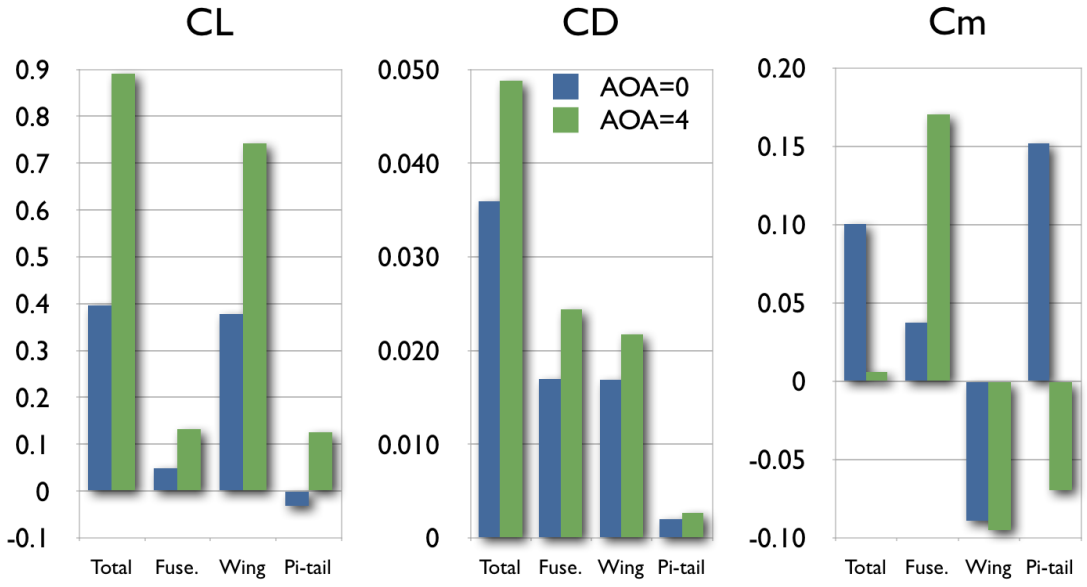


Figure 19: A comparison of the computed loads on the D8 aircraft components.

to $M = 0.6$ with a flight speed of $M = 0.72$ is indeed plausible.

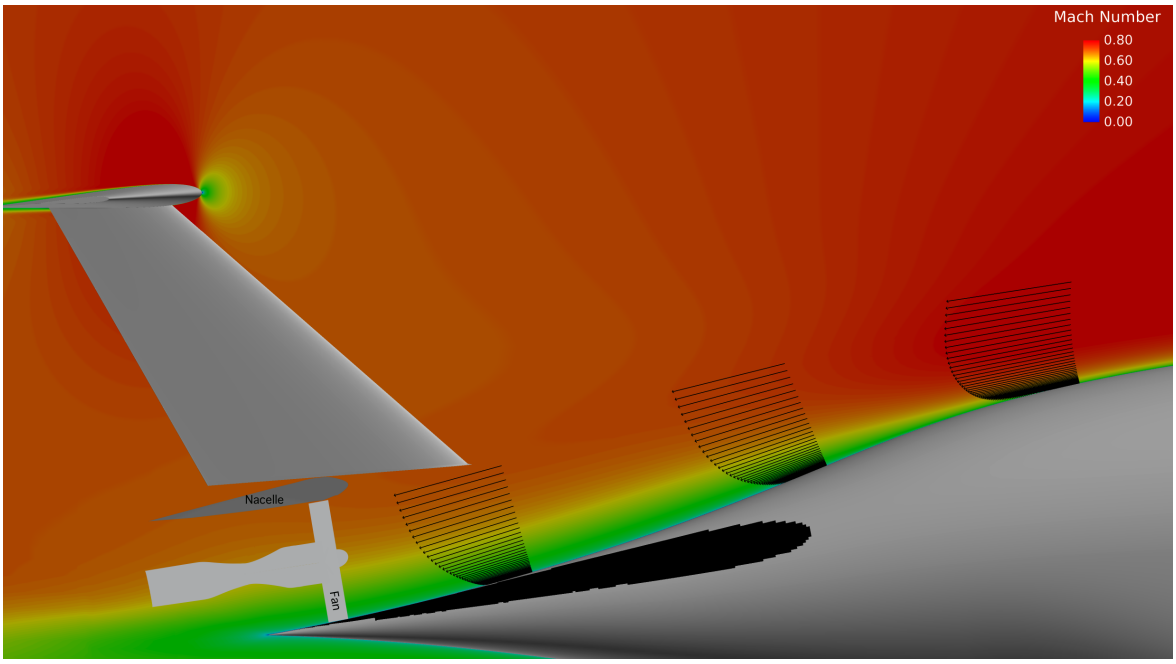


Figure 20: A closeup of the aft end of the D8 aircraft in free-air at M=0.72, $\alpha = 4^\circ$ showing that the shape of the fuselage in the rear acts as a diffuser for the flow entering the fan.

7 Summary and Concluding Remarks

The external aerodynamics of the proposed D8 aircraft is characterized using viscous simulations. Adjoint-based mesh refinement is used with inviscid simulations at low angles of attack as a preliminary check and to guide some aspects of the viscous mesh generation process. The effects of wind tunnel walls and mounting hardware are studied using inviscid simulation and reveal that both the walls and the hardware contribute to changes in lift; however, drag is minimally affected. Mesh parameter sensitivity studies are carried out for the viscous simulations to assess the solution dependence on the mesh. A baseline viscous mesh is used to obtain an alpha sweep on the D8 in the wind tunnel with mounting strut at $M = 0.16$. The results are validated against the Wright Brothers Wind Tunnel test data and it is found that the SST turbulence model predicts lift and drag values that are closer to the WT data. Some preliminary independent assessments of the assertions behind the D8 design are provided and these assertions are found to be justified. The present investigation establishes the groundwork for future studies with a boundary layer ingesting nacelle and engine fan. In future work, the embedded nacelles will be modeled with and without a fan and the aircraft performance will be compared to that with podded nacelles.

Acknowledgements

Support for this work was provided by the Subsonic Fixed Wing (SFW) project of the NASA Fundamental Aeronautics program. The author would like to thank Mike Rogers and Nateri Madavan of NASA Ames Research Center for encouraging this work.

Special thanks to Alejandra Uranga of MIT for answering all my questions about the D8, the MIT wind tunnel tests, for providing photographs of the wind tunnel tests along with wind tunnel data, and for resolving many geometry issues. The author would also like to thank Ed Greitzer, Bob Haimes, and Mark Drela of MIT for useful discussions and the D8 geometry. Finally, the author thanks William Chan, Cetin

Kiris, Thomas Pulliam, and Michael Olsen of NASA Ames for help with Overflow and turbulence modeling, and Michael Aftosmis and Marian Nemec of NASA Ames for help with geometry issues and Cart3D.

References

[1] M. Drela. Development of the D8 Transport Configuration. AIAA Paper 2011–3970, 2011.

[2] E. M. Greitzer et. al. N+3 Aircraft Concepts Designs and Trade Studies, Final Report. NASA CR 2010-216794, 2010.

[3] L. H. Smith Jr. Wake Ingestion Propulsion Benefit. *Journal of Propulsion and Power*, 9(1):74–82, 1993.

[4] [https://github.com/OpenMDAO/EGADS].

[5] M. Nemec and M J. Aftosmis. Adjoint-Based Adaptive Mesh Refinement for Complex Geometries. AIAA Paper 2008–0725, 2008.

[6] W. M. Chan. Overset Grid Technology Development at NASA Ames Research Center. *Computers & Fluids*, 38:496–503, 2009.

[7] P. G. Buning, D. C. Jespersen, T. H. Pulliam, G. H. Klopfer, W. M. Chan, J. P. Slotnick, S. E. Krist, and K. J. Renze. OVERFLOW User's Manual. NASA, 2005.

[8] R. Haimes. Computational Analysis Programming Interface. In *Numerical Grid Generation in Computational Field Simulations*, pages 663–672, 1998.

[9] R. Haimes and M. J. Aftosmis. On Generating High Quality Watertight Triangulations Directly from CAD. In *Numerical Grid Generation in Computational Field Simulations*.

[10] S. A. Pandya and W. M. Chan. Automation of Structured Overset Mesh Generation for Rocket Geometries. AIAA Paper 2009–3993, 2009.

[11] W. M. Chan and J. L. Steger. Enhancements of a Three-Dimensional Hyperbolic Grid Generation Scheme. *Appl. Math & Comp.*, 51:181–205, 1992.

[12] W. M. Chan, R. J. Gomez, S. E. Rogers, and P. G. Buning. Best Practices In Overset Grid Generation. AIAA Paper 2002-3191, 2002.

[13] R. L. Meakin. Object X-rays for Cutting Holes in Composite Overset Structured Grids. AIAA paper 2001–2537, 2001.

[14] R. M. Beam and R. F. Warming. An Implicit Factored Scheme for the Compressible Navier-Stokes Equations. *AIAA Journal*, 16(4):393–402, 1978.

[15] T. H. Pulliam and D. S. Chausse. A Diagonal Form of an Implicit Approximate Factorization Algorithm. *J. Comp. Phys.*, 39(2):347–363, 1981.

[16] P. L. Roe. Characteristic-based schemes for the Euler equations. *Ann. Rev. Fluid Mech.*, 18:337–365, 1986.

[17] E. F. Toro, M. Spruce, and W. Speares. Restoration of the Contact Surface in the HLL Riemann Solver. *Shock Waves*, 4, 1994.

[18] R. H. Nichols, R. W. Tramel, and P. G. Buning. Solver and Turbulence Model Upgrades to OVERFLOW 2 for Unsteady and High-Speed Applications. AIAA paper 2006–2824, 2006.

[19] P. R. Spalart and S. R. Allmaras. A One-Equation Turbulence Model for Aerodynamic Flows. AIAA Paper 92-0439, 1992.

[20] J. A. Bardina, P. G. Huang, and T. J. Coakley. Turbulence Modeling Validation, Testing, and Development. NASA TM-110446, 1997.

[21] F. R. Menter. Two-Equation Eddy-Viscosity Turbulence Models for Engineering Applications. *AIAA Journal*, 32(8):1598–1605, 1994.